

## Article

# Efficient Separation of Photoexcited Charge at Interface between Pure CeO<sub>2</sub> and Y<sup>3+</sup>-Doped CeO<sub>2</sub> with Heterogeneous Doping Structure for Photocatalytic Overall Water Splitting

Honghao Hou <sup>1</sup>, Hirohisa Yamada <sup>2</sup>, Atsumi Nitta <sup>3</sup>, Yoshinori Murakami <sup>4</sup> and Nobuo Saito <sup>1,\*</sup>

<sup>1</sup> Department of Materials Science and Technology, Nagaoka University of Technology, Nagaoka 940-2188, Japan; wily9999@outlook.com

<sup>2</sup> Department of Chemical Engineering, National Institute of Technology Nara College, Nara 639-1080, Japan; yamada@nara.kosen-ac.jp

<sup>3</sup> Department of Environmental Materials, National Institute of Technology Niihama College, Niihama 792-8580, Japan; anitta@mat.niihama-nct.ac.jp

<sup>4</sup> Department of Materials Engineering, National Institute of Technology Nagaoka College, Nagaoka 940-8532, Japan; murakami\_mb@nagaoka-ct.ac.jp

\* Correspondence: saito@analysis.nagaokaut.ac.jp

**Abstract:** Enhancement of photoexcited charge separation in semiconductor photocatalysts is one of the important subjects to improve the efficiency of energy conversion for photocatalytic overall water splitting into H<sub>2</sub> and O<sub>2</sub>. In this study, we report an efficient separation of photoexcited charge at the interface between non-doped pure CeO<sub>2</sub> and Y<sup>3+</sup>-doped CeO<sub>2</sub> phases on particle surfaces with heterogeneous doping structure. Neither non-doped pure CeO<sub>2</sub> and homogeneously Y<sup>3+</sup>-doped CeO<sub>2</sub> gave activities for photocatalytic H<sub>2</sub> and O<sub>2</sub> production under ultraviolet light irradiation, meaning that both single phases showed little activity. On the other hand, Y<sup>3+</sup>-heterogeneously doped CeO<sub>2</sub> of which the surface was composed of non-doped pure CeO<sub>2</sub>, and Y<sup>3+</sup>-doped CeO<sub>2</sub> phases exhibited remarkable photocatalytic activities, indicating that the interfacial heterostructure between non-doped pure CeO<sub>2</sub> and Y<sup>3+</sup>-doped CeO<sub>2</sub> phases plays an important role for the activation process. The role of the interface between two different phases for activated expression was investigated by selective photo-reduction and oxidation deposition techniques of metal ion, resulting that the interface between two phases become an efficient separation site of photoexcited charge. Electronic band structures of both phases were investigated by the spectroscopic method, and then a mechanism of charge separation is discussed.

**Keywords:** overall water splitting; Y<sup>3+</sup>-doped CeO<sub>2</sub> photocatalyst; charge separation at interface; heterogeneous doping structure



**Citation:** Hou, H.; Yamada, H.; Nitta, A.; Murakami, Y.; Saito, N. Efficient Separation of Photoexcited Charge at Interface between Pure CeO<sub>2</sub> and Y<sup>3+</sup>-Doped CeO<sub>2</sub> with Heterogeneous Doping Structure for Photocatalytic Overall Water Splitting. *Materials* **2021**, *14*, 350. <https://doi.org/10.3390/ma14020350>

Received: 22 November 2020

Accepted: 30 December 2020

Published: 12 January 2021

**Publisher's Note:** MDPI stays neutral with regard to jurisdictional claims in published maps and institutional affiliations.



**Copyright:** © 2021 by the authors. Licensee MDPI, Basel, Switzerland. This article is an open access article distributed under the terms and conditions of the Creative Commons Attribution (CC BY) license (<https://creativecommons.org/licenses/by/4.0/>).

## 1. Introduction

Hydrogen is a clean and sustainable carbon neutral fuel with oxygen. In order to make hydrogen as manufactured energy, photocatalytic water splitting into H<sub>2</sub> and O<sub>2</sub> is considered to be one of the most promising approaches for converting solar energy into hydrogen molecules as storage fuel. Photocatalytic water splitting on semiconductor materials has been extensively studied [1–8] since the photocatalytic water splitting on TiO<sub>2</sub> photoelectrodes was discovered in 1972 [9]. In the viewpoint of electronic configuration, discovered photocatalysts are classified into two groups: one is transition metal compounds with d<sup>0</sup> electronic configuration (such as Ti<sup>4+</sup>, Zr<sup>4+</sup>, Nb<sup>5+</sup>, Ta<sup>5+</sup>, W<sup>6+</sup>), the other is typical metal compounds with d<sup>10</sup> electronic configuration (such as Ga<sup>3+</sup>, In<sup>3+</sup>, Ge<sup>4+</sup>, Sn<sup>4+</sup> and Sb<sup>5+</sup>) [1–5]. However, most of the discovered photocatalysts still suffer from relatively low efficiency with a low hydrogen/oxygen production rate, which is not enough for practical application. The process of photocatalytic overall water splitting is separated into three major steps: (i) light absorption to generate photoexcited electrons and holes,

(ii) transfer photoexcited electron and hole to reaction site, and (iii) water reduction and oxidation on the surface. Among these steps, recombination of photoexcited electrons and holes in step (ii) becomes one of causes of low photoenergy conversion. One way to increase the photoenergy conversion is to prevent recombination of photogenerated electrons and holes [1–8]. To support this purpose, crystal defect reduction in photocatalyst is a promising approach because it acts as recombination center. Recently, Domen et al. discovered that photoenergy conversion significantly increased when well-crystalized SrTiO<sub>3</sub> synthesized by the flux method was employed [10], indicating that defect reduction is an effective way to prevent the recombination, and then leads to photocatalytic activity enhancement. As another approach to suppress the recombination, it is considered that the artificial structure formation of charge separation on surfaces is an effective method. For instance, Li et al. reported that the interface between Anatase-TiO<sub>2</sub> and Rutile-TiO<sub>2</sub>,  $\alpha$ -Ga<sub>2</sub>O<sub>3</sub> and  $\beta$ -Ga<sub>2</sub>O<sub>3</sub> plays an important role for separation of photoexcited charge, and then photocatalytic activity was higher than these of single phase [11–13]. The reason why photocatalytic activity enhancement occurs is associated with different electronic structure of both phases. It is considered that photoexcited electron and hole were effectively separated at the interface of both phases because the potential difference of valence band (V.B.) and conduction band (C.B.) act as a driving force of photoexcited charge separation.

CeO<sub>2</sub> is an important rare earth oxide that has been widely applied in many fields, such as solid oxide fuel cell, heterogeneous catalyst, corrosion prevention, ultraviolet absorber and biomaterial because of nontoxicity and excellent chemical stability [14]. For the application in photocatalytic water splitting, Arakawa et al. have reported that CeO<sub>2</sub> has an ability of O<sub>2</sub> evolution from a suspension contained Ce<sup>4+</sup> as an electron acceptor [15]. On the other hand, it is reported that CeO<sub>2</sub> suspension can produce H<sub>2</sub> using S<sup>2-</sup>/SO<sub>3</sub><sup>2-</sup> as hole acceptor [16]. The reagent like Ce<sup>4+</sup> and S<sup>2-</sup>/SO<sub>3</sub><sup>2-</sup> are called sacrificial agents. Therefore, it is desirable that photocatalytic water splitting proceed in pure water. However, no photocatalytic ability of CeO<sub>2</sub> based materials in pure water splitting was reported except for our group, to our best knowledge.

In our previous study, we discovered that Sr<sup>2+</sup>-doped CeO<sub>2</sub> with f<sup>0</sup>d<sup>0</sup> electronic configuration became a new photocatalyst for overall water splitting [17]. Furthermore, we found that Sm<sup>3+</sup>-doped CeO<sub>2</sub> with heterogeneous doping structure has an ability to split water [18]. As a doping metal ion, common characteristics of Sr<sup>2+</sup> and Sm<sup>3+</sup> is that ionic radius of doped metal ion were larger than that of Ce<sup>4+</sup> in fluorite structure, making a stable fluorite lattice based on crystallographic structure [19]. Moreover, as an interesting feature of metal ion doped CeO<sub>2</sub>, neither non-doped pure CeO<sub>2</sub> and homogeneously Sm<sup>3+</sup>-doped CeO<sub>2</sub> showed photocatalytic activities under light irradiation. On the other hand, Sm<sup>3+</sup>-heterogeneously doped CeO<sub>2</sub> of which the surface was composed of non-doped pure CeO<sub>2</sub> and Sm<sup>3+</sup>-doped CeO<sub>2</sub> phases exhibited remarkable photocatalytic activities, indicating that the interface between non-doped pure CeO<sub>2</sub> and Sm<sup>3+</sup>-doped CeO<sub>2</sub> phases plays an important role for the activation process of photocatalytic water splitting [18]. This discovery was characterized by the charge separation at the interface between two phases gave activity enhancement better than each single phase, but more importantly, activated expression with each inert phase for photocatalytic water splitting reaction. However, a mechanism for charge separation and active site generation at the interface between non-doped pure CeO<sub>2</sub> and metal ion doped CeO<sub>2</sub> phases has not been investigated in detail. Therefore, the objective of this study is to confirm whether the interface at both phases become active sites for charge separation. In this study, as a photocatalyst, Y<sup>3+</sup>-doped CeO<sub>2</sub> was prepared to acquire obvious elemental images at the interface between non-doped pure CeO<sub>2</sub> and metal ion doped CeO<sub>2</sub> phase for energy disperse spectroscopic measurement. In case of Sm<sup>3+</sup>-doped CeO<sub>2</sub> in previous study, it was difficult to get clear elemental images at the interface since an energy of characteristic X-ray emitted from Sm had a value closest to that of Ce. This leads to the hindrance of the investigation on photocatalytic active site using selective photo-reduction and photo-oxidation with metal ions. Therefore, the mechanism of charge separation was not discussed in detail. On the

other hand, in case of  $Y^{3+}$ -doped  $CeO_2$ , an energy of characteristic X-ray emitted from Y was quite different from that of Ce. Furthermore, since ionic radius of  $Y^{3+}$  is larger than  $Ce^{4+}$  in  $CeO_2$  [20–26], it is expected that  $Y^{3+}$ -doped  $CeO_2$  shows efficient photocatalytic activity based on the existence of the interface between non-doped pure  $CeO_2$  and  $Y^{3+}$ -doped  $CeO_2$  phase. In the synthesis of  $Y^{3+}$ -doped  $CeO_2$  composed of non-doped pure  $CeO_2$  and  $Y^{3+}$ -doped  $CeO_2$  phase on the surface, a solid state reaction of  $CeO_2$  and  $Y_2O_3$  was used and heated at different calcination temperatures as in a previous report [18]. As a reference, homogeneously  $Y^{3+}$ -doped  $CeO_2$  composed of  $Y^{3+}$ -doped  $CeO_2$  single phase on the surface was prepared by the co-precipitation method. The doping structures of synthesized  $Y^{3+}$ -doped  $CeO_2$  were investigated by X-ray diffraction and energy dispersive spectroscopic methods, and then the relation between the photocatalytic activity and doping structure is discussed. In order to determine the photocatalytic active site, selective photo-reduction of Ru and oxidation deposition of  $PbO_2$  were employed. In addition, the electronic charge separation mechanism is discussed by results of UV-Vis reflectance spectroscopic and ultraviolet photoelectron spectroscopic measurements.

## 2. Materials and Methods

For photocatalyst preparation by the solid state reaction (referred to as SSR) method,  $Y^{3+}$ -doped  $CeO_2$  was prepared by a mixture of  $CeO_2$  (Nacalai Tesque, 99%) and  $Y_2O_3$  (Nacalai) calcinated at different temperatures from 1273 to 1773 K for 16 h under air at atmospheric pressure. After calcination, unreacted residual  $Y_2O_3$  was removed by acid treatment with 0.1 M HCl aqueous solution, and then  $Y^{3+}$ -doped  $CeO_2$  powder was obtained through filtration of the suspension. The molar amount of dissolved- $Y^{3+}$  in filtrate by the acid treatment was determined by inductively coupled plasma optical emission spectroscopy (ICP-OES; ICPS-7510, SHIMADZU, Kyoto, Japan), and then concentration of doped- $Y^{3+}$  in  $CeO_2$  at different calcination temperature was calculated by subtracting the molar amount of dissolved- $Y^{3+}$  from that of initial charge. Prepared  $Y^{3+}$ -doped  $CeO_2$  in SSR at different calcination temperature are referred to as  $xK$ -SSR- ( $x$  represent calcination temperature). As reference sample, pure  $CeO_2$  was calcined at 1573 K for 16 h under air at atmospheric pressure and is referred to as 1573K-Pure- $CeO_2$ . For photocatalyst preparation by co-precipitation (referred to as CPT) method, a mixture of  $Ce(NO_3)_3 \cdot 6H_2O$  (Nacalai Tesque, 99.9%) and  $Y(NO_3)_3 \cdot 6H_2O$  (Nacalai Tesque, 99.9%) at a molar ratio of  $Y/(Y + Ce) \times 100 = 10.0$  mol % was dissolved in distilled water as starting materials. Ammonia aqueous solution (Nacalai Tesque, 28%) was slowly added into prepared solution as a mineralizer with vigorously stirring, and then obtained precursor precipitates were filtrated and dried at 333 K for 12 h under air at atmospheric pressure. Then prepared precursor was calcined at different temperature from 1273 to 1773 K for 16 h under air at atmospheric pressure. Prepared 10 mol %  $Y^{3+}$ -doped  $CeO_2$  in CPT at a different calcination temperature is referred to as  $xK$ -CPT ( $x$  represent calcination temperature). Furthermore, for the preparation of different  $Y^{3+}$ -doping concentrations, mixtures of  $Ce(NO_3)_3 \cdot 6H_2O$  (Nacalai Tesque, 99.9%) and  $Y(NO_3)_3 \cdot 6H_2O$  (Nacalai Tesque, 99.9%) at a molar ratio of  $Y/(Y + Ce) \times 100 = 0.1, 0.5, 1.0, 5.0, 20.0$  and 30.0 mol % were dissolved in distilled water, and precipitates were obtained in a similar fashion. Prepared powders were calcinated at 1573 K for 16 h under air at atmospheric pressure. Prepared samples are referred to as  $xK$ -CPT- $y$ YDC ( $x$  and  $y$  represent calcination temperature and additive molar ratio of Y, respectively).

Powder X-ray diffraction pattern was recorded by X-ray diffractometer (XRD; RINT-2000HF with Cu  $K\alpha$ , Rigaku, Tokyo, Japan) to identify crystal structures of prepared sample. Optical property of prepared samples was obtained by ultraviolet-visible diffuse reflectance spectroscopy (DRS; V570, JASCO, Tokyo, Japan), and energy gap ( $E_g$ ) was calculated by Tauc-plot. BET surface area was measured by nitrogen adsorption and desorption analyzer (Gemini 2360, Micromeritics, SHIMADZU, Kyoto, Japan). Morphology and particle size were observed by a field emission scanning electron microscope (FE-SEM; SU8230, Hitachi High Technologies, Tokyo, Japan) and a scanning transmission electron microscope (STEM; HT7700, Hitachi High Technologies, Tokyo, Japan). Elemental mapping was performed by

FE-SEM and STEM equipped with energy dispersion spectroscopy (EDS; X-Max50, Oxford and Quantax, Bulker, respectively). X-ray photoelectron spectroscopy (XPS; JPS-9010TR, JEOL, Tokyo, Japan) was performed with Mg K $\alpha$  ( $h\nu = 1253.6$  eV) at 10 kV and 10 mA. The energy-level of VBM ( $E_{\text{VBM}}$ ) was investigated by ultraviolet photoelectron spectroscopy (UPS, ESCA 3057, Ulvac-Phi, Tokyo, Japan) with He I excitation (21.2 eV) in 1573K-Pure-CeO<sub>2</sub> and 1573K-CPT-30.0YDC. UPS spectra were recorded at 9 volts-bias in ultrahigh vacuum chamber.

Photocatalytic water splitting was performed by a homemade-closed gas circulation apparatus directly connected to gas chromatograph equipped with a TCD detector (SHIMADZU GC-390B, MS-5A column, Ar was used as carrier gas, Kyoto, Japan). Prior to the photocatalytic water splitting reaction, the prepared photocatalysts were impregnated up to incipient wetness with Ru<sub>3</sub>(CO)<sub>12</sub> (Aldrich Chemical Co., 99%, St. Louis, MO, USA) in THF solution. The amount of RuO<sub>2</sub> was 1.0 wt.% against the prepared sample as Ru meal base. The THF solution was removed under reduced pressure after stirring of the suspension at 333 K for 4 h. The resulting powder was calcinated at 673 K for 4 h under air at atmospheric pressure to oxidize Ru carbonyl complex to RuO<sub>2</sub> as the promoter. In total, 0.3 g of RuO<sub>2</sub>-loaded photocatalysts were suspended in 150 ml of distilled water. Before the water splitting reaction, dissolved gases in suspension were removed by reducing pressure, and 4.0 kPa of Ar was introduced into the reaction system as an inert circulation gas. Then, UV light (source: 300 W Xe lamp) was irradiated through a Pyrex top-irradiation type vessel with vigorous stirring. The amounts of H<sub>2</sub> and O<sub>2</sub> evolution were recorded for 15-min intervals under dark and light irradiation. Wavelength dependence for photocatalytic water splitting was examined by using the same experimental setup, except for cut-off filters (UV35,  $\lambda < 350$  nm; UV36,  $\lambda < 360$  nm; L37,  $\lambda < 370$  nm; L38,  $\lambda < 380$  nm; L39,  $\lambda < 390$  nm; L40,  $\lambda < 400$  nm).

For investigation of the active reduction sites, Ru nanoparticles were photo-deposited in 10.0 vol % methanol and RuCl<sub>3</sub> aqueous solution under light irradiation. In this suspension, methanol works as a hole scavenger to facilitate the deposition of metallic Ru particles, as reported in the literature [27]. On the other hand, for the investigation of the active oxidation site, photo-deposition of PbO<sub>2</sub> was performed in a Pb(NO<sub>3</sub>)<sub>2</sub> aqueous solution under light irradiation. The prepared Ru-deposited and PbO<sub>2</sub>-deposited samples were analyzed by EDS to clarify active sites of reduction and oxidation.

### 3. Results and Discussion

#### 3.1. Doping Structures of Y<sup>3+</sup>-Doped CeO<sub>2</sub> Prepared by SSR and CPT Methods

Figure 1 shows the XRD patterns of Y<sup>3+</sup>-doped CeO<sub>2</sub> fabricated by SSR and CPT methods. 1573K-Pure-CeO<sub>2</sub>(a) showed a well-crystallized fluorite structure without any impurities. In the case of 1573K-CPT(b), the peak position shifted to a higher angle as shown in the expanded figure from 55.6 to 56.8°, indicating that Y<sup>3+</sup> was doped in the crystal lattice of CeO<sub>2</sub> with homogenous doping structures [20–23]. On the other hand, Y<sup>3+</sup>-doped CeO<sub>2</sub> prepared by SSR at different temperatures(c)–(h) showed characteristic diffraction patterns corresponding to heterogeneous doping structures. For Y<sup>3+</sup>-doped CeO<sub>2</sub> prepared by the SSR method, diffraction patterns appeared not only in same position as 1573K-Pure-CeO<sub>2</sub> but also a higher angle in 1573K-SSR (f) and 1673K-SSR (g), meaning that the prepared sample consisted of the non-doped CeO<sub>2</sub> and Y<sup>3+</sup>-doped CeO<sub>2</sub> regions. The intensity of diffraction peaks at a high angle associated with Y<sup>3+</sup>-doped CeO<sub>2</sub> increased with the increasing calcination temperature. Furthermore, these peaks shifted slightly towards a lower angle with an increasing calcination temperature. However, for 1773K-SSR (h) at the maximum temperature, an unclear diffraction peak for the doping phase was observed, but peak broadening on higher angle side occurred, which indicates that Y<sup>3+</sup>-doped CeO<sub>2</sub> exists in low concentrations on the surface. Table 1 summarizes the lattice constant of the Y<sup>3+</sup>-doped phase, the percentage of doped Y<sup>3+</sup> and the percentage of the doped phase obtained by XRD and ICP measurements. Percentages of doped Y<sup>3+</sup> (doped phase) were calculated from their lattice constant according to references [20,21].

On the other hand, percentages of doped  $Y^{3+}$  (Average) were determined by way of ICP measurement as described in the experimental section. For  $Y^{3+}$ -doped  $CeO_2$  prepared by the CPT method, the amount of doped  $Y^{3+}$  (Doped phase) was the same as that of doped  $Y^{3+}$  (average), which means that the prepared  $Y^{3+}$ -doped  $CeO_2$  has a homogeneous doping structure as expected. On the other hand, in the  $Y^{3+}$ -doped  $CeO_2$  prepared by the SSR method, the amount of doped  $Y^{3+}$  (doped phase) was larger than that of doped  $Y^{3+}$  (average), indicating that synthesized  $Y^{3+}$ -doped  $CeO_2$  was composed of non-doped, lower-doped and/or higher-doped  $CeO_2$  with heterogeneous doping structures. Since little diffraction peaks corresponding to the  $Y^{3+}$ -doped phase in 1273K-SSR (f) and 1373K-SSR (g) were observed, surface elemental analysis was performed by using surface sensitive X-ray photoelectron spectroscopic method. As shown in Figure S1, two peaks attributed to  $Y 3d_{5/2}$  and  $Y 3d_{3/2}$  were detected on 1273K-SSR (b) and 1373K-SSR (c) in which little diffraction peaks were observed in XRD measurements. The XPS measurement clearly indicates that all the prepared  $Y^{3+}$ -doped  $CeO_2$  have a  $Y^{3+}$ -doped phase on the topmost surface. Besides,  $Ce 3d_{5/2}$ ,  $Ce 3d_{3/2}$  and their satellite peaks were also detected in all samples. Table 2 shows the  $Y^{3+}$  doping concentration calculated from the peak area of  $Ce 3d_{5/2}$ ,  $Y 3d_{5/2}$  and the corresponding Relative Sensitivity Factor in X-ray photoelectron spectroscopy (XPS; JPS-9010TR, JEOL) and BET specific surface area. In 1573K-CPT, the percentage of doped  $Y^{3+}$  is different from the values determined by XRD and ICP measurements. The reason why the surface  $Y^{3+}$  concentration was 2.4 times larger than that of the bulk is not clear, but it is considered that the topmost surface has an imperceptible dopant distribution in the depth direction. The amount of doped  $Y^{3+}$  on the surface increased with the increasing calcination temperature, then decreased at 1773K. This phenomenon is in good agreement with the  $Sm^{3+}$  doped  $CeO_2$  in our previous study [18], and it is explained that the calcination procedure at high temperatures gives not only an increase in the doping amount but also dopant diffusion from the doped region to non-doped  $CeO_2$ , showing that the doping structure changes from heterogeneous to homogeneous on the surface.

**Table 1.** Lattice constant of doped phase, percentage of doped  $Y^{3+}$  in  $CeO_2$  and percentage of doped phase.

Sample	Lattice Constant of $Y^{3+}$ -Doped Phase/Å	Percentage of Doped $Y^{3+}$ /mol %		Percentage of Doped Phase/% *c
		(Doped Phase) *a	(Average) *b	
1573K-Pure- $CeO_2$	-	-	-	-
1573K-CPT	5.408	10	10	100
1273K-SSR	-	-	1.5	-
1373K-SSR	-	-	2.2	-
1473K-SSR	-	-	3.7	-
1573K-SSR	5.393	44	7.9	11
1673K-SSR	5.396	36	9.4	21
1773K-SSR	-	-	9.8	-

Note: \*a Percentage of doped  $Y^{3+}$  (Doped phase) was calculated from their lattice constant according to references. \*b Percentage of doped  $Y^{3+}$  (Average) was determined by ICP measurement. \*c Percentage of doped phase was obtained by ratio of peak area for pure  $CeO_2(311)$  and  $Y^{3+}$ -doped  $CeO_2(311)$  on the assumption that the crystallinity of both phases was the same.

**Table 2.**  $Y^{3+}$  doping concentration on the surface and specific surface area.

Sample	Percentage of Doped $Y^{3+}$ on Surface (XPS)/mol% <sup>*a</sup>	BET Specific Surface Area/m <sup>2</sup> g <sup>-1</sup>
1573K-Pure-CeO <sub>2</sub>	-	4.3
1573K-CPT	24	0.8
1273K-SSR	6	3.5
1373K-SSR	30	2.4
1473K-SSR	34	2.1
1573K-SSR	42	1.2
1673K-SSR	44	0.8
1773K-SSR	22	0.7

<sup>\*a</sup> Percentage of doped  $Y^{3+}$  in CeO<sub>2</sub> is calculated from XPS.

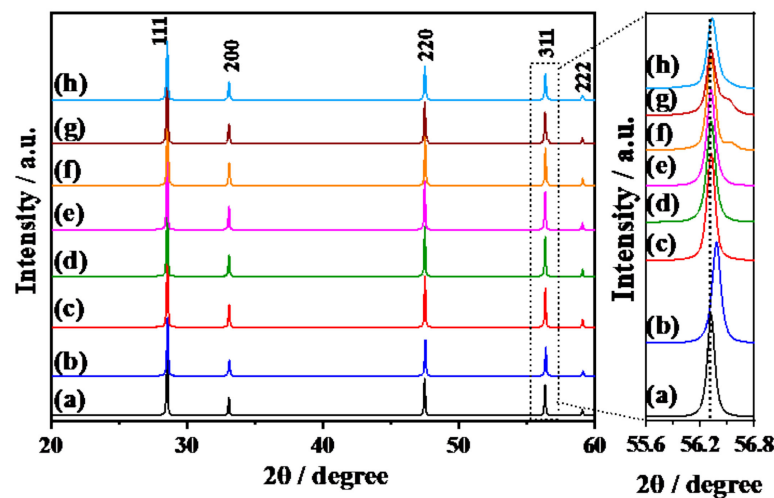


**Figure 1.** X-ray diffraction patterns of 1573K-Pure-CeO<sub>2</sub> (a), 1573K-CPT (b), 1273K-SSR (c), 1373K-SSR (d), 1473K-SSR (e), 1573K-SSR (f), 1673K-SSR (g), and 1773K-SSR (h).

Figure 2 and Figure S2 show FE-SEM /EDS and STEM/EDS images, respectively. In the case of  $Y^{3+}$ -doped CeO<sub>2</sub>(b) prepared by the CPT method, homogeneous distribution structures of the Y element in CeO<sub>2</sub> were clearly observed, which are in good agreement with the results of crystallographic analysis described in the previous section. On the other hand, for  $Y^{3+}$ -doped CeO<sub>2</sub>(c)–(h) synthesized by the SSR method at different calcination temperatures, it was found that the Y element existed in patches, which means Y was heterogeneously doped in CeO<sub>2</sub>. With an increasing calcination temperature, the amount of doped Y increases and then the Y doped area was expanded into non-doped CeO<sub>2</sub> at a high calcination temperature. This phenomenon is also in good agreement with the results of crystallographic analysis. When focusing on the interface between non-doped CeO<sub>2</sub> and  $Y^{3+}$ -doped CeO<sub>2</sub>, the interface area increased with the increasing calcination temperature until nearly 1573 K, reached a maximum of 1573 K, and then decreased due to elemental diffusion from the  $Y^{3+}$  doped CeO<sub>2</sub> to non-doped CeO<sub>2</sub>. In our previous study, in Sm<sup>3+</sup>-doped CeO<sub>2</sub>, we reported that the interface between non-doped CeO<sub>2</sub> and Sm<sup>3+</sup>-doped CeO<sub>2</sub> plays an important role for the activation of the photocatalytic reaction [18]. However, as mentioned in the introduction, it was difficult to get clear interface images of SEM/EDS on Sm<sup>3+</sup>-doped CeO<sub>2</sub>. In this study, in the case of  $Y^{3+}$ -doped CeO<sub>2</sub>, obvious interface images were observed as shown Figure 2e,f.

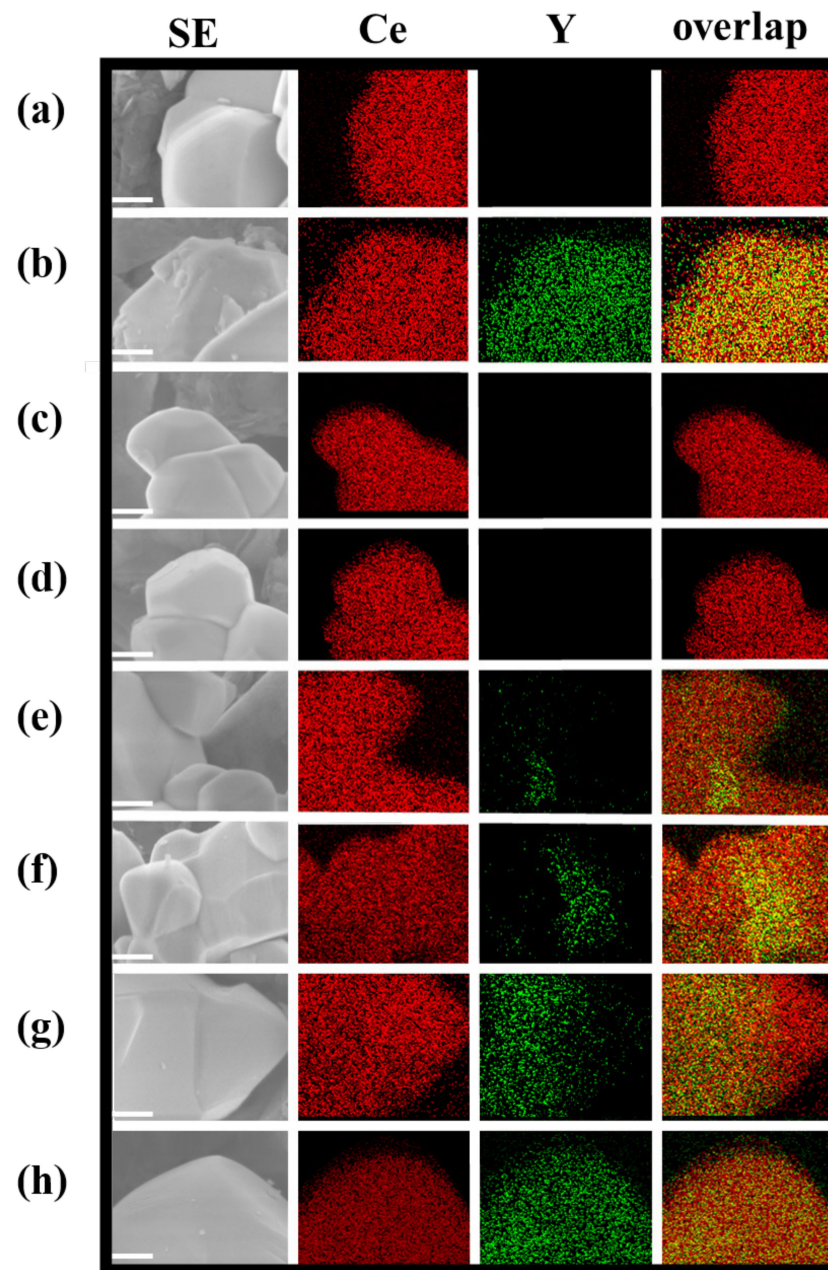


**Figure 2.** FE-SEM/EDS images of 1573K-Pure-CeO<sub>2</sub> (a), 1573K-CPT (b), 1273K-SSR (c), 1373K-SSR (d), 1473K-SSR (e), 1573K-SSR (f), 1673K-SSR (g), and 1773K-SSR (h). Scale bars are 100 nm.

### 3.2. Investigation of Charge Separation Sites by Photo-Deposition Methods

Figure 3 shows FE-SEM/EDS images after photo-deposition of Ru(a) and PbO<sub>2</sub>(b) on photocatalytic active reduction and oxidation sites, respectively. As shown in Figure 3a, little Ru metal was observed in elemental images of pure-CeO<sub>2</sub> and Y<sup>3+</sup> doped CeO<sub>2</sub> prepared by the CPT method. On the other hand, intriguingly, Ru photo-deposition occurred on Y<sup>3+</sup> doped CeO<sub>2</sub> prepared by the SSR method, of which the surface was composed of a heterogeneous doping structure. Ru metal was deposited when the interface of two phases exists on a surface, and they were selectively deposited on the phases of Y<sup>3+</sup> doped CeO<sub>2</sub> near the interface. On the other hand, in the case of PbO<sub>2</sub> deposition as shown in Figure 3b, PbO<sub>2</sub> was selectively deposited on phases of non-doped CeO<sub>2</sub> near the interface.

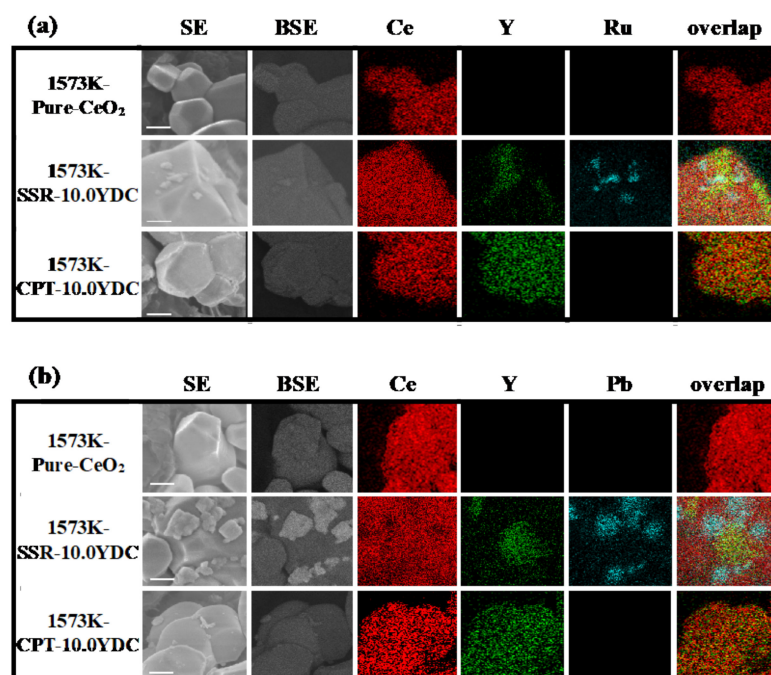


**Figure 3.** FE-SEM/EDS images of 1573K-Pure-CeO<sub>2</sub>, 1573K-SSR and 1573K-CPT. Ru (a) and PbO<sub>2</sub> (b) were photo-deposited on active site. Scale bars are 100 nm.

### 3.3. Photocatalytic Activity for Water Splitting on Y<sup>3+</sup>-Doped CeO<sub>2</sub> with Different Doping Structure

Figure 4 shows the representative photocatalytic water splitting reaction on RuO<sub>2</sub>-loaded Y<sup>3+</sup>-doped CeO<sub>2</sub> prepared by the SSR method at 1573 K. H<sub>2</sub> and O<sub>2</sub> were evolved with a stoichiometric ratio of 2:1 with the light on, which means Y<sup>3+</sup>-doped CeO<sub>2</sub> became an efficient and stable photocatalyst the same as the Sr<sup>2+</sup>-doped CeO<sub>2</sub> [17] and Sm<sup>3+</sup>-doped CeO<sub>2</sub> [18]. Table 3 summarizes the photocatalytic activities for the overall water splitting on the Y<sup>3+</sup>-doped CeO<sub>2</sub> synthesized by CPT and SSR methods at different calcination temperatures with various doping amounts. Photocatalytic activities were normalized by the specific surface area because specific surfaces decreased with increasing calcination temperatures as shown Table 2. In the RuO<sub>2</sub>-loaded 1573K-Pure-CeO<sub>2</sub> without Y<sup>3+</sup> doping, no photocatalytic activity was observed. In addition, RuO<sub>2</sub>-loaded non-doped CeO<sub>2</sub> with different calcination temperatures at 1273–1773 K showed little activity. In the case of RuO<sub>2</sub>-loaded Y<sup>3+</sup>-doped CeO<sub>2</sub> synthesized by the CPT method with homogeneous doping structure, photocatalytic activity was not observed at different calcination temperatures with various doping amounts. On the other hand, RuO<sub>2</sub>-loaded Y<sup>3+</sup>-doped CeO<sub>2</sub> synthesized by the SSR method with a heterogeneous doping structure showed remarkable photocatalytic activity: photocatalytic activity increased with increasing calcination temperatures, reaching a maximum of 1573 K, and then decreased drastically. This phenomenon is in good agreement with our previous reports on Sm<sup>3+</sup>-doped CeO<sub>2</sub> [18], indicating that the heterogeneous doping structure synthesized by the SSR method plays an important role in creating sufficient photocatalytic activity. As shown in Figure 2 and Figure S2, heterogeneous doping structures composed of non-doped and Y<sup>3+</sup> doped phases were observed. It seems that the interface region between non-doped and Y<sup>3+</sup> doped CeO<sub>2</sub> increased with increasing calcination temperatures, reaching a maximum of 1473–1573 K, and then disappeared at above 1673 K monotonically due to the elemental diffusion from Y<sup>3+</sup> doped CeO<sub>2</sub> to non-doped CeO<sub>2</sub>, suggesting that photocatalytic activity was strongly related to the amount of interface between the non-doped and Y<sup>3+</sup> doped phases. Furthermore, since photo-reduction and oxidation sites appeared near these interfaces, as shown in Figure 3, it is suggested that photocatalytic activity is strongly governed by the interface structure on the surface. It is a well-known fact that CeO<sub>2</sub> converts photoenergy to thermal

energy as used in UV absorbed material, which means that photoexcited electrons and holes are rapidly recombined in the process of nonradiative deactivation. In this study, it was discovered that the interface acts as an effective charge separation site of photoexcited electrons and holes with prevention of the nonradiative deactivation process, and leads to efficient photocatalytic activity for the overall water splitting reaction.

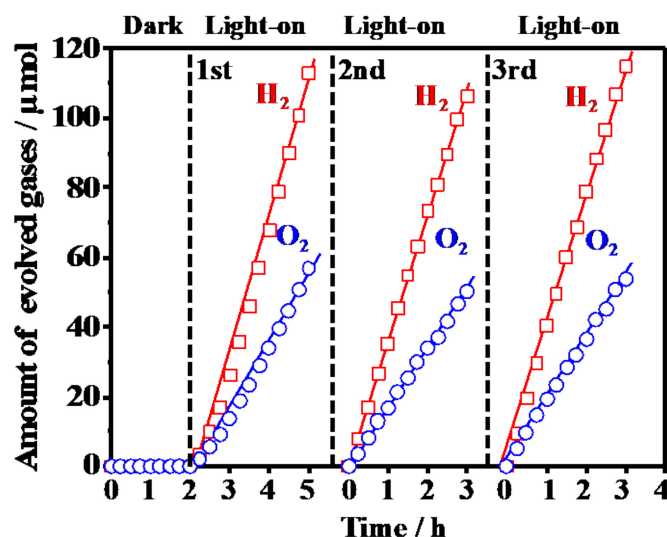


Figure 4. Photocatalytic H<sub>2</sub> and O<sub>2</sub> evolution on RuO<sub>2</sub>-loaded 1573K-SSR without and with light irradiation.

Table 3. Photocatalytic activities for overall water splitting on RuO<sub>2</sub>-loaded Y<sup>3+</sup>-doped CeO<sub>2</sub> synthesized by CPT and SSR methods at different calcination temperature with various doping amounts.

Sample	Doping Structures Determined by XRD and EDS	Activities/ $\mu\text{mol h}^{-1}\text{m}^{-2}$	
		H <sub>2</sub>	O <sub>2</sub>
1573K-Pure-CeO <sub>2</sub>	Non-doped	N.D.	N.D.
1273 K-CPT	Homogeneous	N.D.	N.D.
1373 K-CPT	Homogeneous	N.D.	N.D.
1473 K-CPT	Homogeneous	N.D.	N.D.
1573 K-CPT	Homogeneous	N.D.	N.D.
1673 K-CPT	Homogeneous	N.D.	N.D.
1773 K-CPT	Homogeneous	N.D.	N.D.
1573 K-CPT-0.1YDC	Homogeneous	N.D.	N.D.
1573 K-CPT-0.5YDC	Homogeneous	N.D.	N.D.
1573 K-CPT-1.0YDC	Homogeneous	N.D.	N.D.
1573 K-CPT-5.0YDC	Homogeneous	N.D.	N.D.
1573 K-CPT-20.0YDC	Homogeneous	N.D.	N.D.
1573 K-CPT-30.0YDC	Homogeneous	N.D.	N.D.
1273 K-SSR	Heterogeneous	1.5	0.7
1373 K-SSR	Heterogeneous	5.3	2.6
1473 K-SSR	Heterogeneous	8.5	4
1573 K-SSR	Heterogeneous	30	14.4
1673 K-SSR	Heterogeneous	16.4	7.7
1773 K-SSR	Heterogeneous	3.1	1.5

### 3.4. Electronic Band Structures and Schematic Model of Charge Separation at Interface between CeO<sub>2</sub> and Y<sup>3+</sup>-Doped CeO<sub>2</sub>

Figure 5 shows the UV-Vis diffusion reflectance spectra of 1573K-Pure-CeO<sub>2</sub>(a) and 1573K-CPT-30.0YDC(b), 1573K-SSR(c) and the corresponding Tauc plots(inset). The adsorption edge of the spectrum was approximately 380 nm in 1573K-Pure-CeO<sub>2</sub>(a), on the

other hand, shifted towards a higher wavelength in 1573K-CPT-30.0YDC(b) with a homogeneous  $Y^{3+}$  doping structure. For 1573K-SSR(c), the spectrum was slightly shifted towards a higher wavelength in comparison with that of 1573K-Pure-CeO<sub>2</sub>(a), indicating that this spectrum consists of two phases of nondoped-CeO<sub>2</sub> and  $Y^{3+}$ -doped CeO<sub>2</sub>. As shown in the inserted Tauc plots, the energy gap of 1573K-Pure-CeO<sub>2</sub>(a) and 1573K-CPT-30.0YDC(b) was calculated as 3.30 and 3.20 eV, respectively. Figure 6 shows the excitation wavelength dependence of the photocatalytic H<sub>2</sub> and O<sub>2</sub> evolution on RuO<sub>2</sub>-loaded 1573K-SSR by using a cut-off filter. Photocatalytic activities appeared until around 390 nm, and the dependence of photocatalytic activities is in good agreement with the photo-absorption properties measured by UV-vis diffusion refraction spectra, as shown in Figure 5. In the electronic band structure of CeO<sub>2</sub>, the valence band is mainly composed of O2p orbital, whereas the conduction band mainly consisted of Ce5d orbital. Furthermore, unoccupied Ce4f orbital is located between O2p and Ce5d orbitals. Since the energy gap from O2p to Ce5d and from O2p to Ce4f orbital is 5.0 and 3.4 eV, respectively [28–32], it is realized that the photocatalytic activity is based on the photo-excitation process from O2p to Ce4f. Figure 7 shows the ultra-violet photoelectron emission spectra of 1573K-Pure-CeO<sub>2</sub>(a), 1573K-CPT-30.0YDC(b) and an enlarged view on top of the valence band. In 1573K-CPT-30.0YDC(b), the spectrum was shifted towards the negative direction compared to that of 1573K-Pure-CeO<sub>2</sub>. As shown in the inserted figure, the valence band maximum (VBM) was determined as  $-7.5$  and  $-7.2$  eV vs. the vacuum level, respectively. For 1573K-CPT-30.0YDC(b), broadening was observed on top of the valence band, suggesting the existence of a slight doping distribution on the surface. Matsui et al. reported that the distance of the Ce-O bond in fluorite-CeO<sub>2</sub> decreased with increasing  $Y^{3+}$  doping concentration [33]. Since the Ce-O distance is strongly related to the energy level of O2p orbital, it is suggested that VBM changes by  $Y^{3+}$  doping to CeO<sub>2</sub>. Based on these results, a schematic model of charge separation and efficient overall water splitting at the interface between non-doped and  $Y^{3+}$  doped CeO<sub>2</sub> is shown in Figure 8. Non-doped CeO<sub>2</sub> and  $Y^{3+}$  homogeneously doped CeO<sub>2</sub> showed negligible photocatalytic activities due to the rapid recombination of the photoexcited electron and hole, but efficient charge separation occurs at the interface between two phases because the potential differences of V.B. and C.B. act as driving forces for suppressing the recombination of the photoexcited electron and hole in the process of nonradiative deactivation.

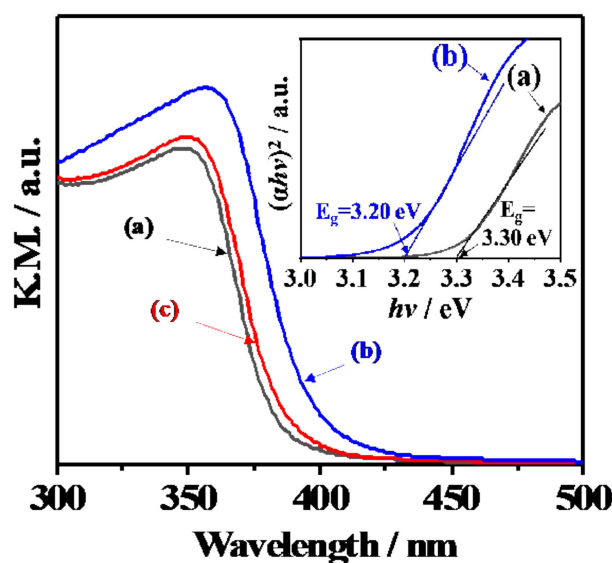


Figure 5. UV-Vis diffuse reflectance spectra of 1573K-Pure-CeO<sub>2</sub> (a), 1573K-CPT-30.0YDC (b), 1573K-SSR (c) and corresponding Tauc plots(inset).

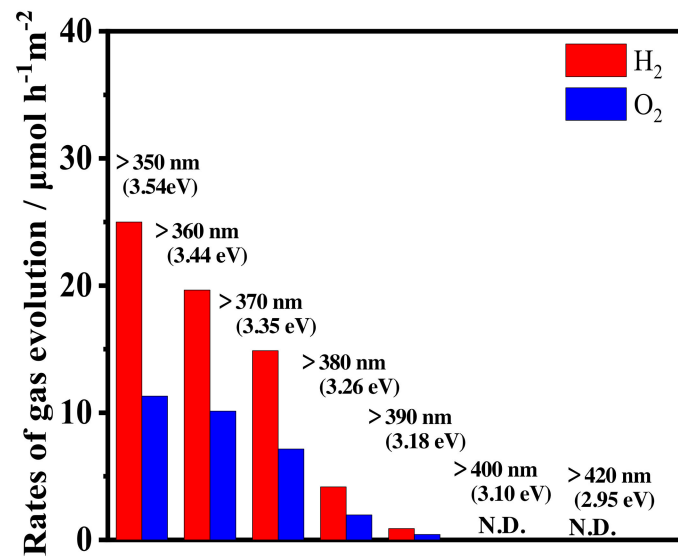


Figure 6. Excitation wavelength dependence of photocatalytic H<sub>2</sub> and O<sub>2</sub> evolution on RuO<sub>2</sub>-loaded 1573K-SSR by using cut-off filters.

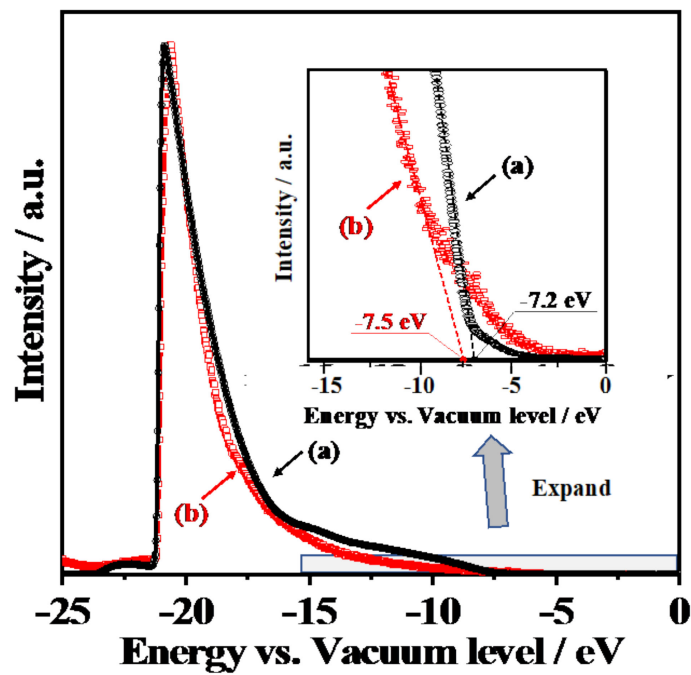
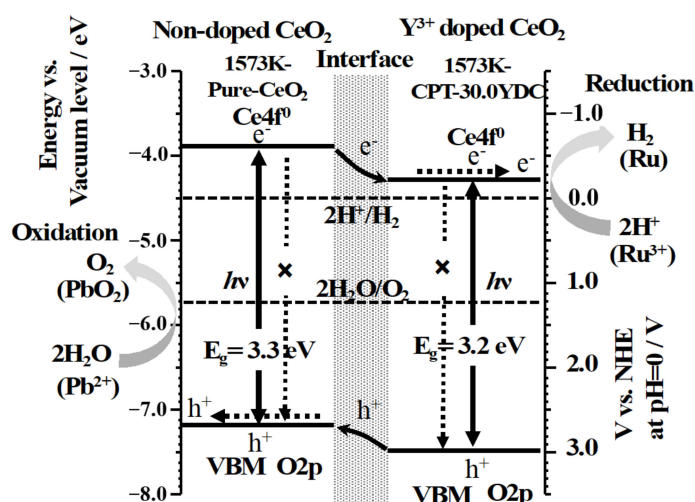


Figure 7. Ultra-violet photoelectron spectra (UPS) of 1573K-Pure-CeO<sub>2</sub> (a) and 1573K-CPT-30.0YDC (b).



**Figure 8.** A schematic model of charge separation and efficient overall water splitting at the interface between 1573K-Pure-CeO<sub>2</sub> and 1573K-CPT-30.0YDC.

#### 4. Conclusions

RuO<sub>2</sub>-loaded Y<sup>3+</sup>-doped CeO<sub>2</sub> composed of non-doped and Y<sup>3+</sup>-doped phases with a heterogeneous doping structure exhibited remarkable photocatalytic activity for overall water splitting. Nevertheless, non-doped and homogeneously Y<sup>3+</sup>-doped CeO<sub>2</sub> showed negligible photocatalytic activity, Y<sup>3+</sup>-doped CeO<sub>2</sub>, of which the surface has an interface of non-doped and Y<sup>3+</sup>-doped phases, showed remarkable photocatalytic activity for overall water splitting. From the selective photo-deposition and spectroscopic measurements, it was found that the interface between non-doped and Y<sup>3+</sup>-doped CeO<sub>2</sub> plays an important role for suppressing the recombination of photoexcited electrons and holes, and led to a sufficient photocatalytic overall water splitting into H<sub>2</sub> and O<sub>2</sub>.

**Supplementary Materials:** The following are available online at <https://www.mdpi.com/1996-1944/14/2/350/s1>, Figure S1: X-ray photoelectron spectra of Ce3d and Y3d for 1573K-CPT (a), 1273K-SSR (b), 1373K-SSR (c), 1473K-SSR (d), 1573K-SSR (e), 1673K-SSR (f), and 1773K-SSR (g), Figure S2: STEM/EDS mapping images of 1573K-Pure-CeO<sub>2</sub> (a), 1573K-CPT (b), 1273K-SSR (c), 1373K-SSR (d), 1473K-SSR (e), 1573K-SSR (f), 1673K-SSR (g), and 1773K-SSR (h). Scale bars are 400 nm.

**Author Contributions:** Conceptualization, N.S.; investigation, H.H.; methodology, H.H.; formal analysis, H.H., A.N., Y.M. and H.Y.; validation, A.N., Y.M. and N.S.; writing—original draft preparation, H.H.; writing—review and editing, N.S., A.N., Y.M.; This study was carried out with the help of all the authors. All authors have read and agreed to the published version of the manuscript.

**Funding:** This research received no external funding.

**Data Availability Statement:** No new data were created or analyzed in this study. Data sharing is not applicable to this article.

**Acknowledgments:** We thank the Nagaoka University of Technology Analysis and Instrumentation Center for use of their facilities and equipment.

**Conflicts of Interest:** The authors declare no conflict of interest.

#### References

- Inoue, Y. Photocatalytic water splitting by RuO<sub>2</sub>-loaded metal oxides and nitrides with d<sup>0</sup>- and d<sup>10</sup>- related electronic configurations. *Energy Environ. Sci.* **2009**, *2*, 364–386. [[CrossRef](#)]
- Kudo, A.; Miseki, Y. Heterogeneous photocatalyst materials for water splitting. *Chem. Soc. Rev.* **2009**, *38*, 253–278. [[CrossRef](#)] [[PubMed](#)]
- Abe, R. Recent progress on photocatalytic and photoelectrochemical water splitting under visible light irradiation. *J. Photochem. Photobiol. C* **2010**, *11*, 179–209. [[CrossRef](#)]

4. Maeda, K. Photocatalytic water splitting using semiconductor particles: History and recent developments. *J. Photochem. Photobiol. C* **2011**, *12*, 237–268. [[CrossRef](#)]
5. Chen, S.S.; Takata, T.; Domen, K. Particulate photocatalysts for overall water splitting. *Nat. Rev. Mater.* **2017**, *2*, 17050–17066. [[CrossRef](#)]
6. Wang, Z.; Inoue, Y.; Hisatomi, T.; Ishikawa, R.; Wang, Q.; Takata, T.; Chen, S.; Shibata, N.; Ikuhara, Y.; Domen, K. Overall Water splitting by Ta<sub>3</sub>N<sub>5</sub> nanorod single crystals grown on the edges of KTaO<sub>3</sub> particles. *Nat. Catal.* **2018**, *1*, 756–763. [[CrossRef](#)]
7. Wang, Z.; Li, C.; Domen, K. Recent developments in heterogeneous photocatalysts for solar-driven overall water splitting. *Chem. Soc. Rev.* **2019**, *48*, 2109–2125. [[CrossRef](#)]
8. Wang, Q.; Domen, K. Particulate photocatalysts for light driven water splitting: Mechanisms, challenges, and design strategies. *Chem. Rev.* **2020**, *120*, 919–985. [[CrossRef](#)]
9. Fujishima, A.; Honda, K. Electrochemical photolysis of water at a semiconductor electrode. *Nature* **1972**, *238*, 37–38. [[CrossRef](#)]
10. Takata, T.; Jiang, J.Z.; Sakata, Y.; Nakabayashi, M.; Shibata, N.; Nandal, V.; Seki, K.; Hisatomi, T.; Domen, K. Photocatalytic water splitting with a quantum efficiency of almost unity. *Nature* **2020**, *581*, 411–414. [[CrossRef](#)]
11. Zhang, J.; Xu, Q.; Feng, Z.; Li, M.; Li, C. Importance of the relationship between surface phases and photocatalytic activity of TiO<sub>2</sub>. *Angew. Chem. Int. Ed.* **2008**, *47*, 1766–1769. [[CrossRef](#)]
12. Wang, X.L.; Li, C. Roles of phase junction in photocatalysis and photoelectrocatalysis. *J. Phys. Chem. C* **2018**, *122*, 21083–21096. [[CrossRef](#)]
13. Wang, X.; Xu, Q.; Li, M.R.; Shen, S.; Wang, X.L.; Wang, Y.C.; Feng, Z.C.; Shi, J.Y.; Han, H.X.; Li, C. Photocatalytic overall water splitting promoted by an  $\alpha$ - $\beta$  phase junction on Ga<sub>2</sub>O<sub>3</sub>. *Angew. Chem. Int. Ed.* **2012**, *51*, 13089–13092. [[CrossRef](#)] [[PubMed](#)]
14. Montini, T.; Melchionna, M.; Monai, M.; Fornasiero, P. Fundamentals and catalytic applications of CeO<sub>2</sub>-based materials. *Chem. Rev.* **2016**, *116*, 5987–6041. [[CrossRef](#)] [[PubMed](#)]
15. Bamwenda, G.R.; Sayama, K.; Arakawa, H. The Photoproduction of O<sub>2</sub> from a Suspension Containing CeO<sub>2</sub> and Ce<sup>4+</sup> Cations as an Electron Acceptor. *Chem. Lett.* **1999**, *28*, 1047–1048. [[CrossRef](#)]
16. Lu, X.H.; Zhai, T.; Cui, H.; Shi, J.Y.; Xie, S.L.; Huang, Y.Y.; Liang, C.L.; Tong, Y.X. Redox cycles promoting photocatalytic hydrogen evolution of CeO<sub>2</sub> nanorods. *J. Mater. Chem.* **2011**, *21*, 5569–5572. [[CrossRef](#)]
17. Kadowaki, H.; Saito, N.; Nishiyama, H.; Inoue, Y. RuO<sub>2</sub>-loaded Sr<sup>2+</sup>-doped CeO<sub>2</sub> with d<sup>0</sup> electronic configuration as a new photocatalyst for overall water splitting. *Chem. Lett.* **2007**, *36*, 440–441. [[CrossRef](#)]
18. Hou, H.H.; Watanabe, K.; Furuno, H.; Nishikawa, M.; Saito, N. Photocatalytic overall water splitting on RuO<sub>2</sub>-loaded Sm<sup>3+</sup>-doped CeO<sub>2</sub> with heterogenous doping structure. *Chem. Lett.* **2018**, *48*, 200–203. [[CrossRef](#)]
19. Yabe, S.; Yamashita, M.; Momose, S.; Tahira, K.; Yoshida, S.; Li, R.; Yin, S.; Sato, T. Synthesis and UV-shielding properties of metal oxide doped ceria via soft solution chemical processes. *Int. J. Inorg. Mater.* **2001**, *3*, 1003–1008. [[CrossRef](#)]
20. Hong, S.J.; Virkar, A.V. Lattice parameters and densities of rare-earth oxide doped ceria electrolytes. *J. Am. Ceram. Soc.* **1995**, *78*, 433–439. [[CrossRef](#)]
21. Rey, J.; Muccillo, E. Lattice parameters of yttria-doped ceria solid electrolytes. *J. Eur. Ceram. Soc.* **2004**, *24*, 1287–1290. [[CrossRef](#)]
22. Dirstine, R.T.; Blumenthal, R.N.; Kuech, T.F. Ionic conductivity of calcia, yttria, and rare earth-doped cerium dioxide. *J. Electrochem. Soc.* **1979**, *126*, 264–269. [[CrossRef](#)]
23. Yang, D.; Wang, L.; Sun, Y.Z.; Zhou, K.B. Synthesis of one-dimensional Ce<sub>1-x</sub>Y<sub>x</sub>O<sub>2-x/2</sub> (0 ≤ x ≤ 1) solid solutions and their catalytic properties: The role of oxygen vacancies. *J. Phys. Chem. C* **2010**, *114*, 8926–8932. [[CrossRef](#)]
24. Lee, W.; Chen, S.Y.; Chen, Y.S.; Dong, C.L.; Lin, H.J.; Chen, C.T.; Gloter, A. Defect structure guided room temperature ferromagnetism of Y-Doped CeO<sub>2</sub> Nanoparticles. *J. Phys. Chem. C* **2014**, *118*, 26359–26367. [[CrossRef](#)]
25. Nolan, M. Charge compensation and Ce<sup>3+</sup> formation in trivalent doping of the CeO<sub>2</sub> (110) surface: The key role of dopant ionic radius. *J. Phys. Chem. C* **2014**, *118*, 6671–6681. [[CrossRef](#)]
26. Murray, A.D.; Murch, G.E.; Catlow, C.R.A. A new hybrid scheme of computer simulation based on Hades and Monte Carlo: Application to ionic conductivity in Y<sup>3+</sup> doped CeO<sub>2</sub>. *Solid State Ion.* **1986**, *18*, 196–202. [[CrossRef](#)]
27. Wang, Q.; Hisatomi, T.; Jia, Q.X.; Tokudome, H.; Zhong, M.; Wang, C.Z.; Pan, Z.H.; Takata, T.; Nakabayashi, M.; Shibata, N.; et al. Scalable water splitting on particulate photocatalyst sheets with a solar-to-hydrogen energy conversion efficiency exceeding 1%. *Nat. Mater.* **2016**, *15*, 611–615. [[CrossRef](#)]
28. Koelling, D.D.; Boring, A.M.; Wood, J.H. The electronic structure of CeO<sub>2</sub> and PrO<sub>2</sub>. *Solid State Commun.* **1983**, *47*, 227–232. [[CrossRef](#)]
29. Pfau, A.; Schierbaum, K.D. The electronic structure of stoichiometric and reduced CeO<sub>2</sub> surfaces: An XPS, UPS and HREELS study. *Surf. Sci.* **1994**, *321*, 71–80. [[CrossRef](#)]
30. Mullins, D.R.; Overbury, S.H.; Huntley, D.R. Electron spectroscopy of single crystal and polycrystalline cerium oxide surfaces. *Surf. Sci.* **1998**, *409*, 307–319. [[CrossRef](#)]
31. Kullgren, J.; Castleton, C.W.M.; Muller, C.; Ramo, D.M.; Hermansson, K. B3LYP calculations of cerium oxides. *J. Chem. Phys.* **2010**, *132*, 054110. [[CrossRef](#)] [[PubMed](#)]
32. Dorenbos, P. The electronic structure of lanthanide doped compounds with 3d, 4d, 5d, or 6d conduction band states. *J. Lumin.* **2014**, *151*, 224–228. [[CrossRef](#)]
33. Yamazaki, S.; Matsui, T.; Ohashi, T.; Arita, Y. Defect structures in doped CeO<sub>2</sub> studied by using XAFS spectrometry. *Solid State Ion.* **2000**, *136*, 913–920. [[CrossRef](#)]